

Supplementary Information

Alloy Oxidation as a Route to Chemically Active Nanocomposites of Gold Atoms in a Reducible Oxide Matrix

P. Sutter,^{1,*} S.A. Tenney,² F. Ivars-Barcelo,² L. Wu,³ Y. Zhu,³ and E. Sutter⁴

¹Department of Electrical and Computer Engineering, University of Nebraska-Lincoln, Lincoln, Nebraska 68588, USA; ²Center for Functional Nanomaterials, Brookhaven National Laboratory, Upton, New York 11973, USA; ³Condensed Matter Physics and Materials Science Department, Brookhaven National Laboratory, Upton, New York 11973, USA; ⁴Department of Mechanical and Materials Engineering, University of Nebraska-Lincoln, Lincoln, Nebraska 68588, USA

1. Morphology of AuSn on Ge support

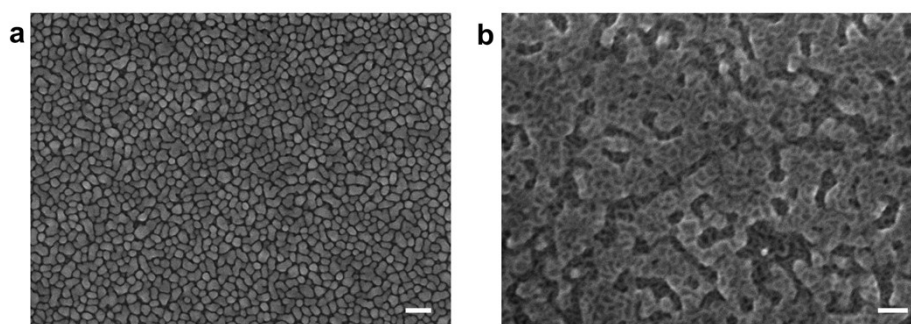


Figure S1. Scanning electron microscopy images of **a.** Sn reference sample, prepared by sputtering 6 nm Sn on Ge. **b.** AuSn sample, prepared by sequential deposition of Au and Sn, both with an equivalent thickness of 6 nm. Scale bars: 100 nm.

2. Atomic-resolution HAADF-STEM of oxidized AuSn nanostructures

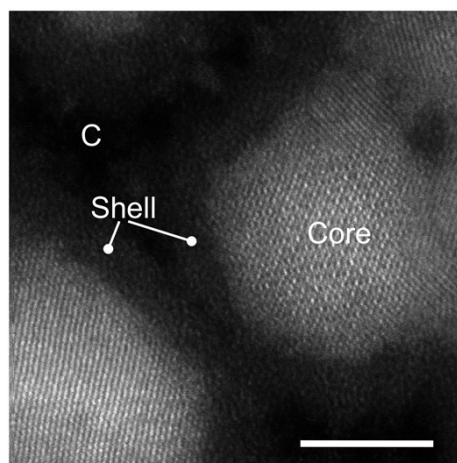


Figure S2. High-resolution high-angle annular dark field (HAADF; Z-contrast) image of oxidized AuSn nanostructures, showing a bright crystalline core (high average atomic number, Z) terminated by an amorphous oxide shell (darker; lower average Z). Outside the oxide shell, the C support is shown dark (lowest Z). Scale bar: 5 nm.

3. Chemical mapping of Sn and O in oxidized AuSn nanostructures by STEM EELS

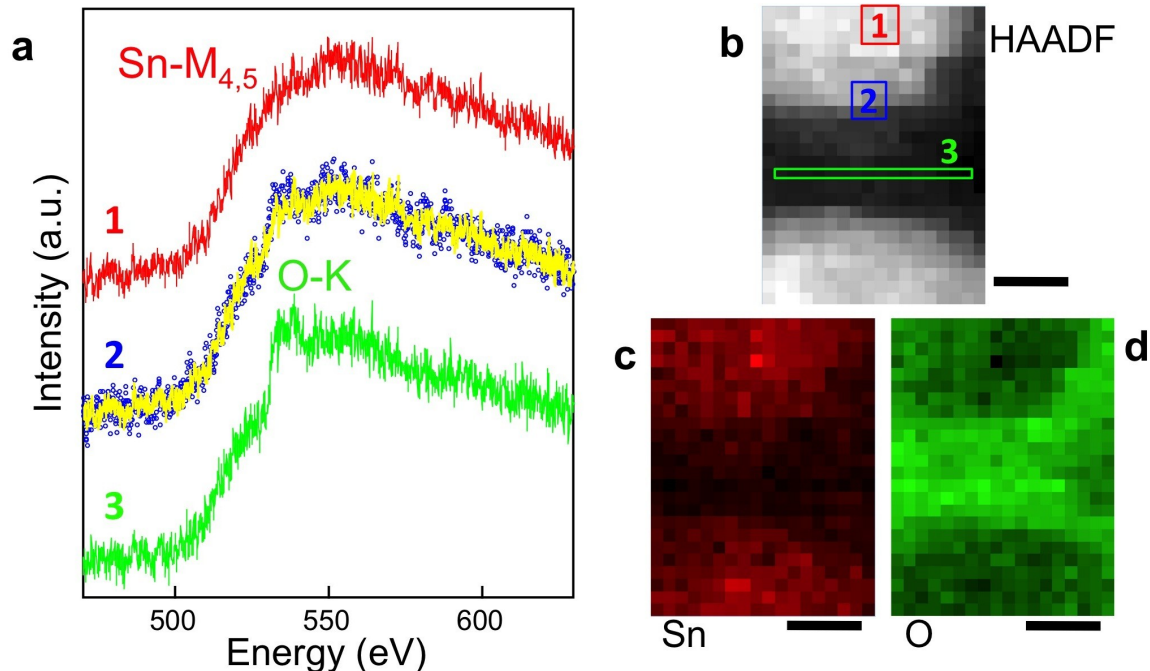


Figure S3. Chemical mapping of Sn and O. **a.** Electron energy loss (EELS) spectra from the acquired spectrum image. The spectra **(1)** (red) and **(3)** (green) are from the corresponding rectangle areas in the high-angle annular dark field (HAADF) image **(b)**, showing the dominant features of the Sn-M_{4,5} edge and the O-K edge. The Au M_{4,5} signal (at 2206 eV) is not shown here. The spectrum **(2)** (blue circles) is from the blue rectangle in **(b)**, and shows a mixture of the Sn-M_{4,5} and O-K edges. We determine the two components (Sn and O distribution) using multiple linear least-squares fitting (MLLS) with a weighted linear combination of spectra **(1)** and **(3)**. The yellow line in **(a)** is the fitted spectrum with weight coefficients of 0.46 and 0.54 for spectrum **(1)** and **(3)**, respectively. **(b)** HAADF image. **(c, d)** The Sn and O distribution maps based on the weighted coefficients. Scale bars in **(b)**-**(d)**: 2 nm.

4. XPS data

Fig. S4 gives time-dependent XPS measurements of Sn 3d_{5/2} and Au 4f core levels of a nanostructured AuSn alloy on Ge support. Sn 3d_{5/2} spectra of the AuSn alloy were measured at different times during oxidation at room temperature in air, and compared with the time evolution for a reference sample of pure Sn nanoparticles, prepared at the same time and exposed to the same oxidation conditions. The Au 4f spectra for the AuSn alloy were also measured over the same time intervals, and are compared with the Au 4f spectrum of a bulk Au foil, used as a reference sample. The raw data (black symbols) were deconvoluted by fitting to Gaussian-Lorentzian products after subtraction of a Shirley-type background. For the Sn 3d_{5/2} spectra, dark and light blue shaded areas indicate the fit components corresponding to oxidized Sn and metallic Sn⁰, respectively. The Au 4f spectra could be fitted by single Gaussian-Lorentzians for the 4f_{5/2} and 4f_{7/2} peaks, which are shifted by a constant energy relative to the Au reference due to alloying with Sn. No oxidized Au was detectable in the Au 4f spectra.

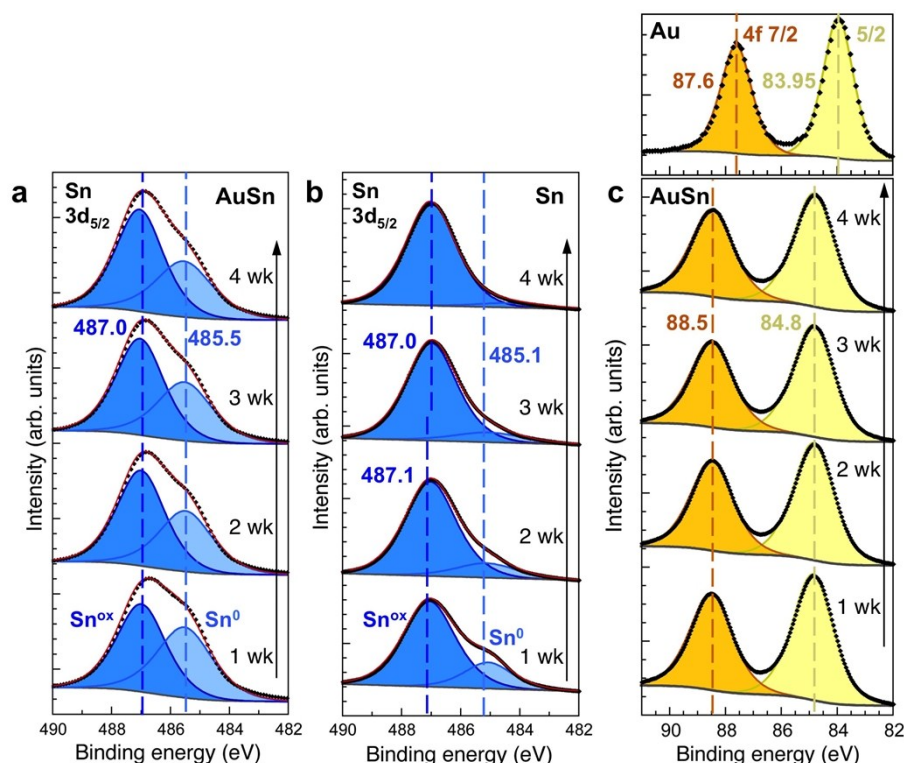


Figure S4. **a.** Sn $3d_{5/2}$ XPS of a nanostructured AuSn alloy, exposed at room temperature to air for different durations. Oxidation times (from bottom to top, see arrows): 1 week, 2 weeks, 3 weeks, 4 weeks. **b.** Same for a bulk Sn reference sample. For both AuSn^{ox} and Sn^{ox}, the Sn $3d_{5/2}$ peaks can be deconvoluted into two components at binding energies of 485–485.5 eV (metallic Sn⁰) and 487 eV (Sn oxide), respectively. In both cases, the Sn⁰ component decreases with progressive exposure to air. **c.** Au 4f XPS of a nanostructured AuSn alloy, exposed at room temperature to air for different durations. Oxidation times (from bottom to top, see arrow): 1 week, 2 weeks, 3 weeks, 4 weeks. Topmost panel: Au foil reference spectra.

5. Additional XPS spectra & quantification of the [O]:[Sn] ratio in the oxide shell

In addition to the Au 4f and Sn 3d photoelectron spectra, we also followed the O 1s core level during the progressive oxidation of nanostructured AuSn alloys on Ge support. O1s XPS spectra of AuSn after room temperature oxidation in air for 1 – 4 weeks are shown in Figure S5a. The asymmetric peaks can be deconvoluted into two components, a lower binding energy peak at 530.6 eV characteristic of the O 1s core level in Sn-oxides and a peak at ~532 eV associated with Ge-oxides formed on the Ge support.

The ratio of the integrated XPS intensities of the Sn $3d_{5/2}$ peak corresponding to Sn in the oxide shell and of the O 1s component corresponding to Sn-oxide (shaded areas in Figure S5b) was used to quantify the composition of the amorphous oxide shell of room temperature oxidized AuSn nanostructures, in particular to determine the [O]:[Sn] atomic ratio. Our previous work on the oxidation of pure Sn nanoparticles at room temperature has shown the formation of an amorphous Sn(II) oxide (i.e., SnO) shell (E. Sutter et al., *Part Part Syst Char* **31**, 879 (2014)), but the presence of Au in our AuSn samples could modify the stoichiometry of the oxide shell. Our quantification shows that this is indeed the case. Based on the integrated intensities of the relevant O 1s and Sn $3d_{5/2}$ components

and taking into account the relative sensitivity factors (RSF = 0.66 for O 1s; RSF = 4.3 for Sn 3d_{5/2}; C.D. Wagner et al., *Surf. Interface Anal.* **3**, 211 (1981)), we find an [O]:[Sn] atomic ratio of 1.3 for a sample oxidized for 4 weeks in air. This suggests that the oxidation of AuSn at room temperature leads to the formation of non-stoichiometric amorphous oxides comprising Sn, O, and Au.

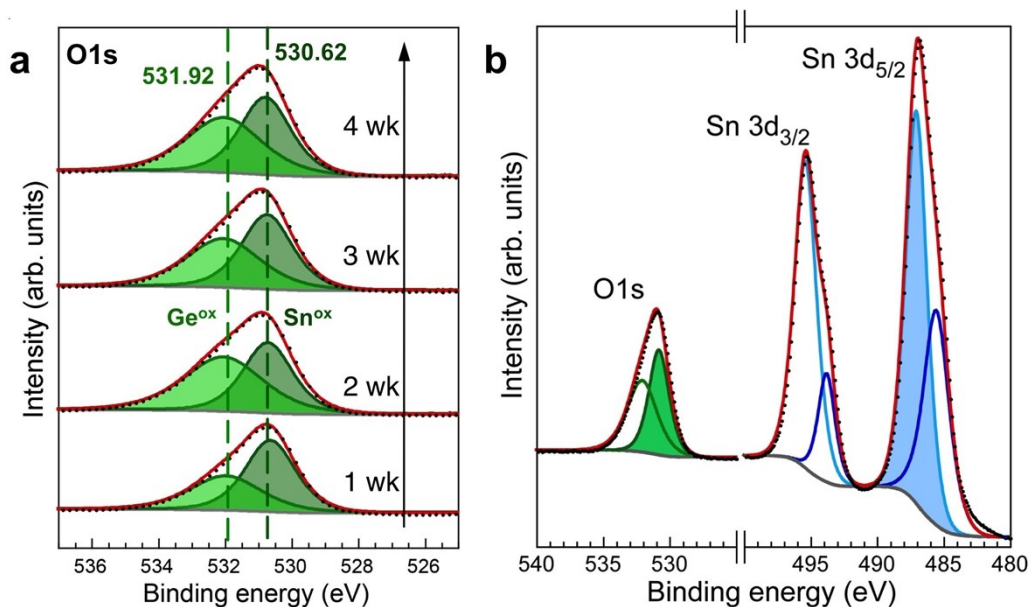


Figure S5. a. Progression of the O1s XPS peak during oxidation of AuSn nanostructures on Ge support at room temperature in air for 1 – 4 weeks. **b.** O1s and Sn3d core levels at $t = 4$ weeks. The components used for quantification of the [O]:[Sn] atomic ratios are shaded light green (O1s) and light blue (Sn3d_{5/2}).

Finally, we note that the above quantification is insensitive to possible adsorbed O₂ on the surface of our samples. Previous XPS spectra by Kawabe et al. (*Surf. Sci.* **448**, 101 (2000)) for O₂ adsorbed on reduced (i.e., sub-stoichiometric) SnO₂ at room temperature showed an O1s peak centered at ~532.6 eV. Our measurements (Fig. S5) do not detect significant spectral intensity at this binding energy, but are readily deconvoluted into only two contributions: a broader peak from Ge-oxide and a narrower peak from Au-Sn oxide. The latter, well-separated from the expected location of the O1s peak from adsorbed O₂, was used to quantify the composition of the amorphous oxide shells around Au-Sn nanoparticles. Hence, our quantification would not be affected by contributions from adsorbed O₂.

6. Oxide thickness determination from XPS peak ratios

The thickness of the growing oxides (Fig. 2b of the paper) has been calculated from the measured XPS peak ratios. The analysis was based on laboratory XPS data, obtained with Al K α excitation ($h\nu = 1486.6$ eV). With this excitation, based on the universal curve the inelastic mean free path of Sn 3d photoelectrons is $\lambda \sim 1.4$ nm. Even though the Au-Sn oxide is non-stoichiometric with a composition of \sim SnO_{1.3} (see above), we used the mass density of SnO (6.45 g·cm⁻³). The mass density of SnO₂ (6.85 g/cm³) is only ~6% higher,

i.e., using the density of SnO does not cause any errors within the statistical significance of our data.

The oxide thickness on oxidized AuSn and β -Sn samples was determined from the ratio between the Sn 3d 5/2 intensities of Sn⁰ and Sn²⁺ (Fig. S4).

Oxide thickness determination for the β -Sn reference sample: For β -Sn we use the molar mass $M_{\text{Sn}} = 118.7 \text{ g}\cdot\text{Mol}^{-1}$ and density $7.365 \text{ g}\cdot\text{cm}^{-3}$; for SnO the molar mass M_{SnO} is $134.7 \text{ g}\cdot\text{Mol}^{-1}$ and the density $6.45 \text{ g}\cdot\text{cm}^{-3}$. From these values, we find molar densities of Sn ($\rho_{\text{Sn}} = 0.062 \text{ Mol}\cdot\text{cm}^{-3}$) and of Sn in SnO ($\rho_{\text{SnO}} = 0.048 \text{ Mol}\cdot\text{cm}^{-3}$).

We derive the thickness of the SnO like surface oxide on Sn nanostructures by integrating the contributions of the oxide shell (thickness h_{ox}) and remaining metal core to the total Sn 3d 5/2 XPS intensity, taking into account the inelastic mean free path, λ :

$$I(d, h) = \int_d^{d+h} \exp(-x/\lambda) dx$$

To determine the oxide thickness, we used the following equation:

$$R = A(\text{Sn}^{2+}) / [A(\text{Sn}^{2+}) + A(\text{Sn}^0)] = \rho_{\text{SnO}} I(0, h_{\text{ox}}) / [\rho_{\text{SnO}} I(0, h_{\text{ox}}) + \rho_{\text{Sn}} I(h_{\text{ox}}, r)].$$

Here, $A(\text{Sn}^{2+})$ and $A(\text{Sn}^0)$ denote the areas (determined by peak fitting) of the 3d 5/2 peaks corresponding to Sn²⁺ and Sn⁰, respectively; $\rho(\text{Sn})$ and $\rho(\text{SnO})$ are the molar densities of Sn in β -Sn and in Sn(II) oxide; r is the thickness of the metallic core of the nanostructures, determined from TEM to be $(12 \pm 2) \text{ nm}$; and $I(d, h)$ is as defined above. The oxide thickness, h_{ox} , was determined by numerically solving the above equation in the software package *Mathematica*.

Oxide thickness determination for AuSn: In analyzing the thickness of the surface oxide on AuSn, we used two limiting scenarios: (i) *complete phase separation*, i.e., formation of a pure SnO shell and concentration of the Au in the metallic core; and (ii) *totally suppressed phase separation*, i.e., formation of an oxide shell with unchanged atomic ratio of Au and Sn.

The analysis in both cases follows that described above for Sn oxidation, but with different values of the Sn molar densities:

(i) *Complete phase separation:*

- Sn density in SnO_{1.3}: $\rho_{\text{SnOx}} = 0.046 \text{ Mol}\cdot\text{cm}^{-3}$.
- Sn density in AuSn: $\rho_{\text{AuSn}} = 0.053 \text{ Mol}\cdot\text{cm}^{-3}$.

(ii) *Suppressed phase separation:*

- Sn density in Au-SnO_{1.3}: $\rho_{\text{SnOx}} = 0.023 \text{ Mol}\cdot\text{cm}^{-3}$.
- Sn density in AuSn: $\rho_{\text{AuSn}} = 0.053 \text{ Mol}\cdot\text{cm}^{-3}$.

The analysis shows a significantly reduced oxidation rate for AuSn than for the Sn reference sample (see Fig. 2 of the paper).

7. Detection of Au in the growing surface oxide shell of AuSn nanostructures

Measurements of the time dependent intensity of the Au 4p 3/2 core level, which provides a significantly reduced photoelectron escape depth and hence higher surface

sensitivity compared to Au 4f, were used to detect if Au remains embedded in the growing oxide and to quantify its amount. XPS measurements were compared with simulations in two limiting cases: (i) *complete phase separation*, i.e., formation of a pure SnO shell and enrichment of Au in the metallic core; and (ii) *completely suppressed phase separation*, i.e., formation of a Au-Sn oxide shell with unchanged concentration ratio of the two metals (here 1:1).

Our experiment followed the attenuation of the Au 4p 3/2 peak during oxidation of AuSn over a period of 4 weeks. To simulate the data, we calculated the expected Au 4p 3/2 signal, based on the atomic densities Au in the two limiting cases. In case of *complete phase separation*, a pure SnO shell would form, and as the shell grows thicker it progressively attenuates the Au 4p intensity originating entirely in the metallic core. In case of *suppressed phase separation*, Au 4p intensity originates in both the oxide shell and the metal core, taking into account the different density of Au atoms in the oxide and alloy.

To simulate the two scenarios, we integrated the contributions of the alloy core and oxide shell to the overall Au 4p signal, assuming an inelastic mean free path $\lambda \sim 1.4$ nm determined from the universal curve. The analysis used the formalism described in section 2., with the following molar densities of Au in the different phases:

(i) *Complete phase separation:*

- Au density in SnO_{1.3}: $\rho_{\text{SnOx}} = 0$.
- Au density in AuSn: $\rho_{\text{AuSn}} = 0.053 \text{ Mol}\cdot\text{cm}^{-3}$.

(ii) *Suppressed phase separation:*

- Au density in Au-SnO_{1.3}: $\rho_{\text{SnOx}} = 0.023 \text{ Mol}\cdot\text{cm}^{-3}$.
- Au density in AuSn: $\rho_{\text{AuSn}} = 0.053 \text{ Mol}\cdot\text{cm}^{-3}$.

The analysis summarized in Fig. 2c of the paper shows that phase separation is nearly completely suppressed at the initial stages of oxidation. At a later stage the overall Au content of the oxide decreases. However, a pure SnO shell is never achieved but instead an oxide containing both Sn and Au is formed, as shown also in chemical mapping in (S)TEM.

8. Mass spectroscopy analysis of near-ambient pressure CO-to-CO₂ conversion

The reaction $\text{CO} + \frac{1}{2} \text{O}_2 \rightarrow \text{CO}_2$ was probed at room temperature by dosing different gas mixtures (CO + O₂) at near-ambient pressures into a ultrahigh vacuum chamber and analyzing the reaction product (CO₂) using a sampling capillary (0.75 mm bore) brought into close vicinity (< 1 mm) of the surface. A constant partial pressure of O₂ (0.1 Torr) was maintained in the chamber while the CO partial pressure was varied in steps from ~0 (i.e., the CO background pressure in the UHV system) to 2 Torr. The partial pressures for masses 28 AMU (CO), 32 AMU (O₂), and 44 AMU (CO₂) were followed by mass spectrometry. Raw data for all measured sample composition are shown in Figure S5.

The data shown in the paper (Fig. 4) represent steady-state values of the CO to CO₂ conversion efficiency, calculated from measurements at masses 28 AMU and 44 AMU recorded after the gas pressures were stable to < 5% following each change in the CO flow rate. The analysis assumes that all gas molecules that enter the sampling capillary originate from the sample surface, i.e., are either molecules backscattered or desorbed (as

Supplementary Information: "Alloy Oxidation as a Route to Chemically Active Nanocomposites of Gold Atoms in a Reducible Oxide Matrix" 6

reaction products or unreacted) from the sample. The CO to CO₂ conversion efficiency η is computed from the measured ratio of masses 44 AMU (CO₂) and 28 AMU (CO and CO₂ fragments; assuming a negligible N₂ background, which we verified independently) via:

$$\eta = I_{44\text{AMU}} / (I_{28\text{AMU}} - 0.11 \cdot I_{44\text{AMU}}),$$

where we have subtracted from the 28 AMU signal the contribution from cracked CO₂ molecules, according to the cracking pattern of CO₂:

(Mass/relative intensity): 44/100; 28/11; 16/9; 12/6; 45/1.

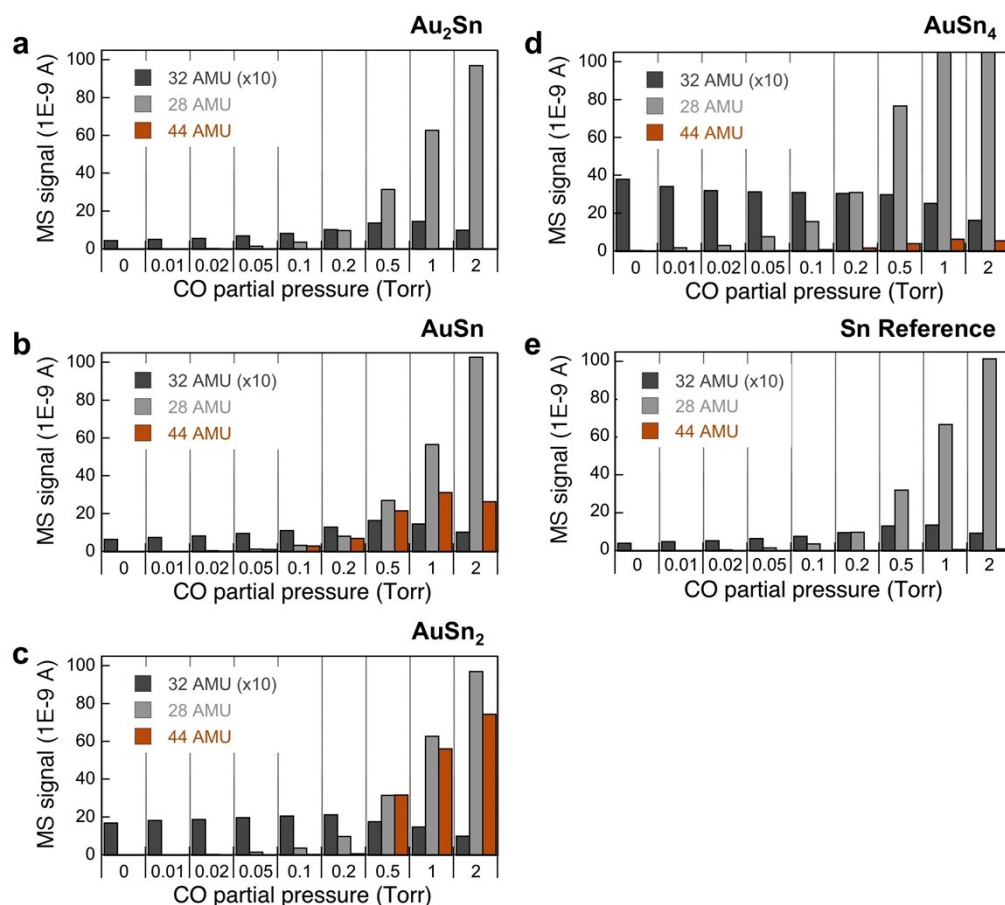


Figure S6. Mass spectrometer signals (masses 28, 32, and 44 atomic mass units, AMU) for gases evolving from samples exposed 0.1 Torr O₂ and different partial pressures of CO. The gases were sampled by a capillary (0.75 mm inner diameter) brought to within 1 mm from the sample surface. Different bimetallic Au-Sn alloys, oxidized at room temperature in air, were probed: **a.** Au₂Sn; **b.** AuSn; **c.** AuSn₂; and **d.** AuSn₄. **e.** Reference sample of oxidized Sn nanostructures.

The gray shaded bars in Fig. 4 in the paper represent the as-calculated values of the conversion efficiency for the different samples studied. Note that there is some scatter in the oxygen pressure from sample to sample (see Fig. S6; nominal pO₂ = 0.1 Torr; actual pO₂ ranging from 0.1 – 0.3 Torr), but this variability did not affect our conclusions

because of the way the measurements were conducted (sampling at fixed O₂ partial pressure and at different CO partial pressures) and because the reported conversion efficiencies were computed from actual (measured) partial pressures of the reactants. The analysis of the CO to CO₂ conversion efficiency described above assumes that the active phase of our (Au-Sn)-oxide catalysts covers the entire sample surface. But this tends to significantly underestimate the actual efficiency because the active catalyst, the dewetted and then oxidized Au_xSn_{1-x} alloy, covers only a fraction of the surface of the Ge support. This is illustrated in Fig. S7. In the left half of the TEM image shown in Fig. S7b the inactive exposed Ge support is highlighted in red, whereas the active oxidized Au-Sn alloy nanostructures are shown in gray.

From Fig. S7b, the actual surface area covered by the active (Au-Sn)-oxide catalyst is estimated to be ~70% of the total sample area. We have taken this into account by multiplying the measured efficiency values by an appropriate correction factor (1.43). The corrected values are given as orange colored bars in Fig. 4 of the paper. For completeness, we are reporting in Fig. 4 both the uncorrected (gray) and corrected (orange) values, as illustrated in Figure S7a.

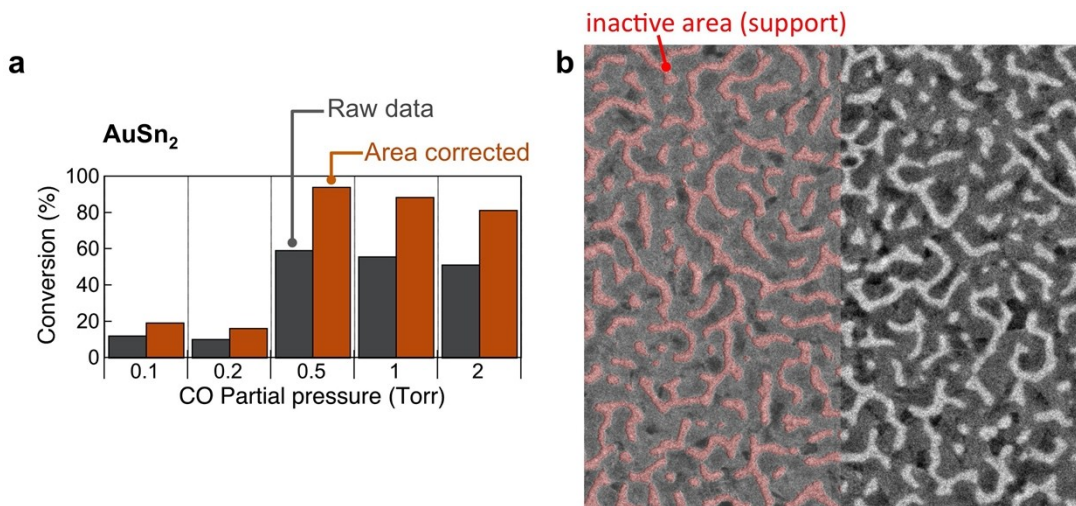


Figure S7. Geometric correction of the measured CO to CO₂ conversion efficiency to account for the partial surface coverage of the active oxidized Au-Sn alloy phase. **a.** Illustration of the data representation in fig. 4 of the manuscript. **b.** TEM image illustrating the areas covered by the active phase and by the exposed Ge support (shaded red on the left hand side of the micrograph).

9. Reversible CO adsorption in low-energy ion scattering spectroscopy (LEIS)

To further support the suggested CO oxidation reaction pathway – a mechanism in which embedded Au atoms provide active low-coordinated Au sites for adsorption of CO and reaction to CO₂ with oxygen from the surrounding oxide surface – we performed LEIS measurements during CO exposure of an oxidized AuSn sample. These measurements are summarized in Fig. S8.

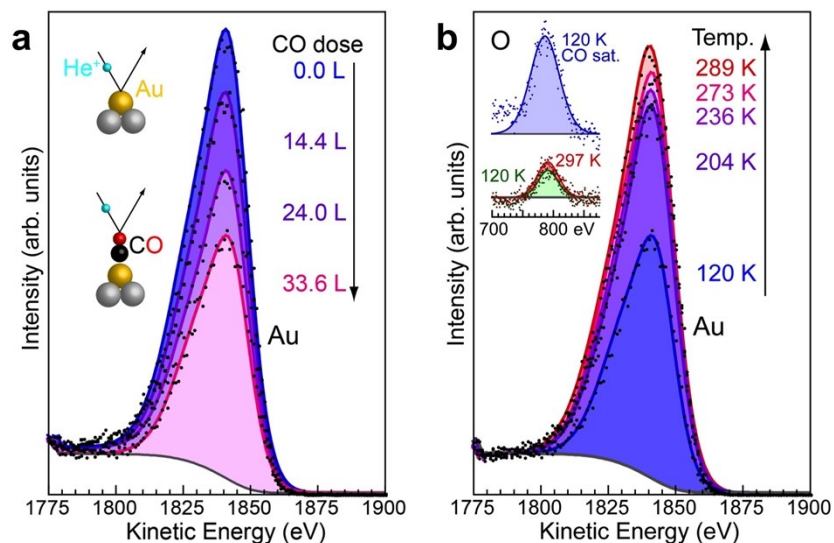


Figure S8. LEIS during reversible CO adsorption. **a.** LEIS signal from Au during CO dosing (pressure: 2×10^{-7} Torr, sample temperature: 120 K). Progressive reduction of the Au signal due to shadowing of Au sites by adsorbed CO (inset). Right: Cumulative CO dose. **b.** Recovery of the Au LEIS signal during thermal desorption of CO in vacuum, shown on the same scale as the data in a. Right: Sample temperatures. Inset: oxygen LEIS spectra at 120 K before CO adsorption (green), after 33.6 L CO dose (blue), and after desorption of CO by heating to 297 K (red). The increase in the O LEIS signal is consistent with C binding to Au (i.e., exposure of O) during CO adsorption.

LEIS measurements in CO were carried out at minimal total He^+ dose on the sample to suppress the modification by sputtering by the low-energy ions. Adsorption of CO at a sample temperature of 120 K causes a progressive decrease in the LEIS signal from Au, consistent with the shadowing of Au by adsorbed CO molecules (Figure S8a). The reversibility of the adsorption is shown by LEIS measurements during heating of the sample from 120 K to room temperature (Figure S8b). In this process, the intensity of the Au LEIS signal recovers to >97% of the original intensity prior to CO adsorption, demonstrating the nearly complete desorption of CO from the Au sites close to room temperature. Comparing the oxygen LEIS signal before and after CO adsorption, as well as after thermal desorption, we observe a distinct increase in the intensity upon CO adsorption due to the binding of CO in a way (C down) that projects the O atom toward vacuum. As with the Au LEIS signal, this change is completely reversible upon thermal desorption of CO from the surface. Our observations are consistent with molecular adsorption of CO at Au surface sites, and relatively weak binding with binding energy of the order of a few $k_B T$ at room temperature.